

# GAMMA-RAY BURST PROMPT EMISSION LIGHT CURVES AND POWER DENSITY SPECTRA IN THE ICMART MODEL

BO ZHANG (张博)<sup>1,2,3</sup> AND BING ZHANG (张冰)<sup>2</sup>

*Draft version June 27, 2018*

## ABSTRACT

In this paper, we simulate the prompt emission light curves of gamma-ray bursts (GRBs) within the framework of the Internal-Collision-induced MAGnetic Reconnection and Turbulence (ICMART) model. This model applies to GRBs with a moderately high magnetization parameter  $\sigma$  in the emission region. We show that this model can produce highly variable light curves with both fast and slow components. The rapid variability is caused by many locally Doppler-boosted mini-emitters due to turbulent magnetic reconnection in a moderately high  $\sigma$  flow. The runaway growth and subsequent depletion of these mini-emitters as a function of time define a broad slow component for each ICMART event. A GRB light curve is usually composed of multiple ICMART events that are fundamentally driven by the erratic GRB central engine activity. Allowing variations of the model parameters, one is able to reproduce a variety of light curves and the power density spectra as observed.

*Subject headings:* Stars: gamma-ray burst: general

## 1. INTRODUCTION

A gamma-ray burst (GRB) event comprises two phases, prompt emission and afterglow. The prompt  $\gamma$ -ray emission is usually highly variable, with many pulses overlapping within a short duration (Fishman & Meegan 1995). The power density spectra (PDSs) of the light curves are typically a power law with a possible turnover at high frequencies (Beloborodov et al. 2000). The light curves may be decomposed as the superposition of an underlying slow component and a more rapid fast component (Gao et al. 2012). The fast component tends to be more significant in high energies, and becomes less significant at lower frequencies (Vetere et al. 2006).

It has been shown that the external shock model has difficulty producing GRB variability while maintaining a high radiative efficiency (Sari & Piran 1997; cf. Dermer & Mitman 1999). The detection of the steep decay phase following GRB prompt emission (Tagliaferri et al. 2005) suggests that the prompt emission region is detached from the afterglow emission region (Zhang et al. 2006). This nails down the internal origin of GRB prompt emission for the majority of GRBs.

For an internal origin of GRB prompt emission, the variability is usually attributed to the erratic activity of the central engine (e.g., Rees & Mészáros 1994; Kobayashi et al. 1997). It is envisaged that the ejecta launched from the central engine is composed of multiple shells with variable bulk Lorentz factors. Faster late shells catch up and collide with slower early shells. Part of the kinetic energy of the ejecta is converted to energy of non-thermal particles in these internal shocks, a fraction of which is released as the observed non-thermal radiation. In this model, different variability timescales are related to the angular spreading time of colliding shells at different internal shock radii. In order to account for superposed slow and fast variability components, one has to assume that the central engine itself carries these two variability components in the time history of jet launching (Hascoët et al. 2012),

whose physical origin is unclear. The internal shock model also suffers a list of criticisms (e.g., Zhang & Yan 2011 for a review), including low radiation efficiency (e.g., Kumar 1999; Panaitescu et al. 1999), fast cooling (Ghisellini et al. 2000; Kumar & McMahon 2008),<sup>4</sup> particle number excess (Daigne & Mochkovitch 1998; Shen & Zhang 2009), inconsistency with some empirical relations (Amati et al. 2002; Zhang & Mészáros 2002; Liang et al. 2010), and overpredicting the brightness of the photosphere emission component (Daigne & Mochkovitch 2002; Zhang & Pe'er 2009).

Alternatively, the GRB variability can be interpreted as locally Doppler-boosted emission in a relativistic bulk flow, such as relativistic mini-jets (Lyutikov & Blandford 2003; Yamazaki et al. 2004) or relativistic turbulence (Narayan & Kumar 2009; Kumar & Narayan 2009; Lazar et al. 2009) in a bulk relativistic ejecta. Some criticisms have been raised to these models. For example, relativistic turbulence damps quickly so that the emission from the turbulence cannot be sustained (Zrake & MacFadyen 2012). The simulated light curves are composed of well-separated sharp pulses without an underlying slow component (Narayan & Kumar 2009; Lazar et al. 2009). Also the pulse was calculated to have a symmetric shape for the turbulence model (Lazar et al. 2009), which is in contradiction with the data.

Recently, Zhang & Yan (2011, hereafter ZY11) proposed an Internal-Collision-induced MAGnetic Reconnection and Turbulence (ICMART) model to explain prompt emission of GRBs. Like the traditional internal shock scheme, the ICMART model envisages internal interactions of shells within the ejecta wind. The main difference is that the ejecta is Poynting flux dominated, with the magnetization parameter  $\sigma \equiv F_p/F_m > 1$  in the collision region, where  $F_p$  and  $F_m$  are Poynting flux and matter flux, respectively. This was motivated by the non-detection of a bright photosphere thermal component in GRB 080916C (Zhang & Pe'er 2009) and most

<sup>1</sup> School of Astronomy and Space Science, Nanjing University, Nanjing 210093, China; bozhang@physics.unlv.edu

<sup>2</sup> Department of Physics and Astronomy, University of Nevada Las Vegas, Las Vegas, NV 89154, USA

<sup>3</sup> Purple Mountain Observatory, Chinese Academy of Sciences, Nanjing 210003, China

<sup>4</sup> This problem is recently alleviated by Uhm & Zhang (2013), who showed that by introducing magnetic field decay as the outflow streams outward, the fast cooling spectrum can be harder than the traditional  $F_\nu \propto \nu^{-1.5}$  spectrum. However, a requirement is that the emission region has to be large where the magnetic field is weak. This corresponds to an unconventional internal shock radius, but is consistent with the ICMART model.

other Large Area Telescope GRBs (Zhang et al. 2011). For a helical magnetic field structure, the initial collisions only serve to distort the magnetic field configurations. As multiple collisions proceed, the field configurations would be distorted to a critical point when a cascade of reconnection and turbulence occurs. Charged particles can be accelerated in these reconnection regions, leading to intense gamma-ray radiation. Within this model, a GRB light curve is supposed to have two variability components: a broad (slow) component that tracks central engine activity, and an erratic (fast) component with multiple sharp pulses superposed on the slow component, which is related to numerous reconnection sites during the ICMART event.

In this paper, we simulate GRB light curves and their corresponding PDSs within the framework of the ICMART model. In Section 2 we describe the basic model and the simulation method. The simulation results are presented in Section 3. Section 4 summarizes the findings with some discussion.

## 2. BASIC SCHEME AND SIMULATION METHODS

We first summarize the basic ideas of the ICMART model (ZY11). Magnetized shells with initial  $\sigma > 1$  are envisaged to collide, leading to distortion of magnetic field lines until a threshold is reached and a runaway magnetic dissipation is triggered. During such an ‘‘avalanche’’-like reconnection/turbulence cascade, it is envisaged that fast reconnection seeds in the moderately high  $\sigma$  regime would inject moderately relativistic outflows in the emission regions (ZY11; Lyubarsky 2005), which would excite relativistic turbulence. The turbulence would facilitate more reconnection events, which trigger further turbulence. The magnetic energy is converted to particle energy and efficient radiation. During the growth of the reconnection/turbulence cascade, the number of reconnection sites as observed at any instant increases rapidly with time, so that multiple mini-emitters contribute simultaneously to the observed gamma-ray emission. Rapid evolution of individual reconnection sites leads to rapid variability of the observed GRB light curves. The cascade stops as  $\sigma$  drops around or below unity when most magnetic energy is converted into radiation or kinetic energy. During the growth of an ICMART event, turbulence is not quickly damped due to the continuous injection of particle energy from the reconnection events, which continuously drives turbulence.

With these preparations, we can model the light curve of a GRB within the framework of the ICMART model. Lacking full numerical simulations of magnetic turbulence and reconnection, in this paper we perform a Monte Carlo simulation based on some simplest assumptions. We define each reconnection event as a fundamental mini-emitter, which carries a local Lorentz boost with respect to the bulk of the emission outflow. Each reconnection event can be modeled as a pulse, which can be bright and spiky if the mini-emitter beams toward the observer, but dim and broad if the mini-emitter beams away from the observer’s direction. The observed light curve is the superposition of the emission from all these mini-emitters. For simplicity, we assume that the characteristic brightness (peak luminosity) of each reconnection event in the rest frame of the reconnection outflow is the same. We also take the shape of each pulse as a Gaussian form for simplicity (e.g., Narayan & Kumar 2009; Lazar et al. 2009). Our goal is to try to simulate the superposed slow and fast components, and the precise shape of each pulse does not matter too much. In any case, we note that the shape of a spike within the ICMART model is mainly defined by the time history of each

reconnecting mini-jet rather than the time history of an ideal eddy, so the pulse profile may not necessarily be symmetric with peak time. This is different from the previous models (Narayan & Kumar 2009; Lazar et al. 2009) that invoke relativistic turbulence.<sup>5</sup> More importantly, the shape of a broad pulse in the model is asymmetric: the rising portion is defined by the timescale of the reconnection-turbulence cascade process, while the decay portion is controlled by high-latitude emission after the ICMART cascade ceases.

There are three rest frames in this model: the first is the rest frame of the mini-jet, i.e. the outflow of the individual reconnection event. These mini-jets are moving with a relative Lorentz factor  $\gamma$  with respect to the jet bulk. We denote parameters in this frame as ( $''$ ). The second frame is the rest frame of the jet bulk, which moves with a Lorentz factor  $\Gamma$  with respect to the central engine. We denote parameters in this frame as ( $'$ ). The third one is the rest frame of the observer (with the cosmological expansion effect ignored). The quantities within these three frames are connected through two Doppler factors, i.e.,

$$\mathcal{D}_1 = [\Gamma(1 - \beta_{\text{bulk}} \cos \theta)]^{-1} \quad (1)$$

and

$$\mathcal{D}_2 = [\gamma(1 - \beta \cos \phi)]^{-1}, \quad (2)$$

where  $\beta_{\text{bulk}}$  and  $\beta$  are the corresponding dimensionless velocities with respect to  $\Gamma$  and  $\gamma$ , respectively,  $\theta$  is the latitude of the mini-jet with respect to the line of sight (i.e. the angle between the line of sight and the radial direction of the bulk ejecta at the location of the mini-jet), and  $\phi$  is the angle between the mini-jet direction and radial direction of the ejecta bulk within the comoving frame of the ejecta bulk.

Each reconnection event is supposed to give rise to a single pulse in the GRB light curve. Since several reconnection events may occur simultaneously, some pulses can superpose with each other. For a naive Sweet-Parker reconnection,<sup>6</sup> one has (e.g., see Zweibel & Yamada 2009 and references therein)

$$v'_{\text{in}} L' = v'_{\text{out}} r', \quad (3)$$

where  $v'_{\text{in}}$  is the inflow velocity of the reconnection layers,  $v'_{\text{out}}$  is the outflow velocity, and  $r'$  and  $L'$  are the width and length of the reconnection layer, respectively. Reconnection physics demands  $v'_{\text{in}} \ll v'_{\text{out}}$ , so that  $r' \ll L'$ . On the other hand, what defines the duration of the reconnection event is the thickness of the bunch of magnetic field lines that continuously approach each other, and we assume that it is also of the order of  $L'$ . As a result, in the bulk comoving frame (the  $'$  frame), the duration of each pulse can be approximated as  $\Delta t' = L'/v'_{\text{in}}$ . In the observer frame, this is translated to  $\Delta t = \Delta t'/\mathcal{D}_1$ , which corresponds to the duration of a certain pulse in the observer frame.

For simplicity, we assume that the radiation intensity arising from each reconnection event has the same spectral form, i.e., the Band function (see Band et al. 1993), in the comoving

<sup>5</sup> Even for turbulence, the previous simulations invoked a circular eddy, while MHD turbulence eddies are highly distorted, especially in small scales (Goldreich & Sridhar 1995; Cho, Lazarian & Vishniac 2003). This would reduce the symmetry of the pulse shapes in the turbulence models. As a result, we consider the symmetry issue raised by Lazar et al. (2009) would not be relevant for the ICMART model.

<sup>6</sup> In reality, the Sweet-Parker prescription is too simple. Rapid reconnection is achieved in an X-point geometry with turbulence playing an essential role (e.g. Lazarian & Vishniac 1999). The simple treatment here only offers an order of magnitude estimate.

frame of the mini-jet (the  $''$  frame),

$$I_{\nu''}'' \propto \left(\frac{\nu''}{\nu_0''}\right)^\alpha \left(1 + \frac{\nu''}{\nu_0''}\right)^{\beta-\alpha}. \quad (4)$$

The observed flux can be calculated as

$$F_\nu = \int \mathcal{D}_1^3 \mathcal{D}_2^3 I_{\nu''}'' d\Omega \approx \mathcal{D}_1^3 \mathcal{D}_2^3 I_{\nu''}'' \frac{r'^2 \cos\theta}{D^2}, \quad (5)$$

where  $D$  is the distance of the GRB to the observer.

In a high- $\sigma$  flow,  $v'_{\text{out}}$  can eventually reach a relativistic speed (with Lorentz factor  $\gamma$ ), and  $v'_{\text{in}}$  can reach a maximum value of  $0.1c$  (e.g. Lyubarsky 2005 and references herein). Therefore,  $r' \sim 0.1L'$ . The Lorentz factor of the mini-jet is related to  $\sigma$  and would drop to unity when  $\sigma$  drops below unity. The detailed dependence is related to the complicated physics of relativistic reconnection. In this paper, we adopt  $\gamma \propto (1+\sigma)^{1/2}$  (i.e.,  $\gamma$  is proportional to the relativistic Alfvén Lorentz factor). We also investigated other dependences between  $\gamma$  and  $(1+\sigma)$ . The general conclusions regarding how the simulated light-curve properties depend on various parameters are essentially similar. In the rest of the paper, we only focus on the  $\gamma \propto (1+\sigma)^{1/2}$  assumption.

In the simulations, we fix the Band function parameters as the following:  $\alpha = -1$ ,  $\beta = -3$ , and the peak frequency  $\nu''$  is chosen such that  $\langle \mathcal{D}_1 \mathcal{D}_2 \rangle h\nu'' \sim 300$  keV is satisfied, where 300 keV is the typical observed value of GRB spectral peak, and  $\langle \mathcal{D}_1 \mathcal{D}_2 \rangle$  is the average value of the product of the two Doppler factors. Based on these assumptions, we calculate the received flux in the detector band of *Swift* Burst Alert Telescope (BAT; i.e., 15 - 150 keV).

In our Monte Carlo simulation, four random parameters have been introduced. They are: (1) comoving length of the reconnection region  $L'$ , which is assumed to either have a typical value or have a power-law distribution with index  $-5/3$  below a typical value; (2) the mini-jet direction (angle  $\phi$  with respect to the bulk motion direction) in the bulk comoving frame, which is taken as isotropic or a Gaussian distribution with respect to  $\phi = 90^\circ$  (see more discussion below); (3) the latitude of a mini-jet  $\theta$  with respect to the viewing direction, which is random within the cone of the jet opening angle; and (4) the epoch when a mini-jet occurs, which is taken to satisfy a distribution of exponential growth with time, i.e.  $N(t) \propto 2^{t/t_0}$ . The total number  $N$  of the mini-jets is a free parameter, which is defined by the requirement that they dissipate most magnetic energy in the local emission regions, so that the local  $\sigma$  is brought to below unity after each ICMART event.<sup>7</sup> Assuming that the magnetic energy density is roughly uniform within the emission region, this number can be simply written as the ratio between the total dissipated volume (i.e., total volume multiplied by the filling factor  $f$ ) and the volume of the region affected by each reconnection event that powers a mini-jet. Within the  $1/\Gamma$  cone, this number is

$$N \approx f \frac{4\pi R^2 \frac{R}{\Gamma} \pi \frac{1}{\Gamma^2}}{L'^3}, \quad (6)$$

<sup>7</sup> The average  $\sigma$  of the ejecta can be still above unity, if the filling factor  $f \ll 1$ , since the majority of magnetic energy is still not dissipated. A small  $f$  seems to be required by the central engine study of Lei et al. (2013), who obtained  $\sigma$  values greater than the measured typical Lorentz factors of GRBs (Liang et al. 2010).

where  $R$  is the radius of the emission region from the central engine.

Other input parameters include the radius of the emission region  $R$ , the jet opening angle  $\theta_j$ , the initial values of  $\Gamma$ , and  $\sigma$  (which defines the initial  $\gamma$ ). For each reconnection event, we assume that half of the dissipated magnetic energy is released in the form of photons, while the other half is deposited to the jet bulk and used to boost the kinetic energy of the bulk.<sup>8</sup> Therefore,  $\Gamma$ ,  $\sigma$ , and  $\gamma$  are all functions of time during each ICMART event.

The exponential growth of magnetic dissipation eventually ends when the local  $\sigma$  drops around or below unity. Without numerical simulations, it is unclear how abrupt the ending process is. In this paper we just assume an abrupt cessation of the cascade process, so that the number of new mini-jets drops to 0 after a particular time. The observed ‘‘tail’’ emission after this epoch is therefore contributed by the high-latitude emission from other mini-jets not along the line of sight due to the ‘‘curvature effect’’ delay. This delay timescale is calculated as  $t_{\text{delay}} = R(1-\mu)/c$  with respect to the last emission along the line of sight, where  $\mu = \cos\theta$ . We calculate the contribution of all the mini-jets within  $\theta_j = 5^\circ$ . Although most of the received emission comes from the mini-jets within the  $1/\Gamma$  cone, those mini-jets outside the  $1/\Gamma$  cone make some contribution to the high-latitude emission. We calculate the delay timescale of each mini-jet, apply its Doppler factor to calculate the amplitude and shape of the pulse, and superpose these mini-jets to get the curvature tail of each ICMART event.

### 3. SIMULATION RESULTS

#### 3.1. Sample Light Curves

We run a series of Monte Carlo simulations to generate sample light curves. We first focus on the light curves for only one ICMART episode. The light curve of one GRB could be then modeled by superposing multiple ICMART events.

We first take the following nominal parameters:  $R = 5 \times 10^{15}$  cm,  $L' = 5 \times 10^{11}$  cm,  $\Gamma_{\text{ini}} = 200$ ,  $\gamma_{\text{ini}} = 3$ , and  $N \approx 50,000$ . Considering an exponential growth, i.e., that each reconnection seed would eject a bipolar outflow and would stir up the ambient medium to trigger two reconnection events, one may estimate the generation number of successive reconnection events,  $n \approx 14.6$ , through the requirement  $N \approx \sum^n 2^n = 50,000$ . The timescale for each generation in the bulk comoving frame may be estimated as  $L'/v'_{\text{in}} \sim 10$  s, which corresponds to an observer frame timescale  $t_0 \sim 0.1$  s. This is the typical ‘‘e-folding’’ timescale. The total duration (rising timescale) of an ICMART event is therefore  $n$  times larger, i.e.  $t_r = nt_0 \sim 1.5$  s, which we adopt in the simulations. We also assume that the observer’s line of sight is along the jet axis, and we take a redshift  $z = 0$  for simplicity.<sup>9</sup> For a power-law distribution of  $L'$ , in principle,  $L'$  can extend to much smaller values. In our simulations, reconnection regions with  $L' < 5 \times 10^9$  cm are not considered, since the observed durations of these events already meet the detector’s variability limit. In the following we test various factors that may affect the shape of the light curves.

<sup>8</sup> Half of the dissipated energy is initially deposited as heat, and then gets converted to kinetic energy due to adiabatic expansion (Drenkhahn & Spruit 2002).

<sup>9</sup> Varying redshifts effectively stretches the light curves, and samples different spectral segments in the intrinsic spectrum. We show below that the light curve shape does not sensitively depend on the spectral regime. So the redshift factor plays a minor role in defining the shape of light curves.

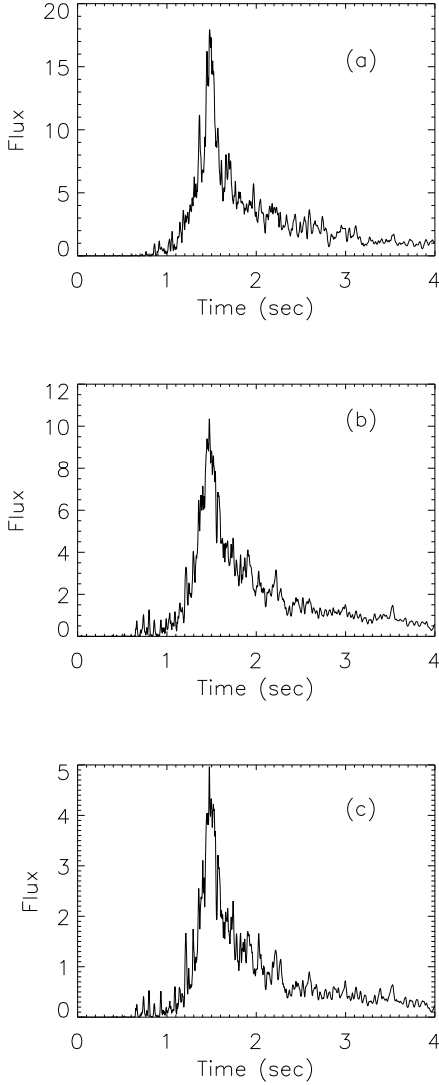


FIG. 1.— Simulated light curves of one ICMART event with the following parameters:  $R = 5 \times 10^{15}$  cm,  $L' = 5 \times 10^{11}$  cm,  $\Gamma_{\text{ini}} = 200$ , and  $\gamma_{\text{ini}} = 3$ ,  $N = 50,000$ , and rising time  $t_r \sim 1.5$  s. The three panels correspond to different  $\phi$  distributions: (a) isotropic; (b) Gaussian  $\phi$ -distribution with a typical angle  $45^\circ$  with respect to plane perpendicular to the bulk motion direction; (c) Gaussian  $\phi$ -distribution with a typical angle  $30^\circ$ .

### 3.1.1. Distribution of the Mini-jet Directions

We first test how the simulated light curve depends on the unknown distribution of  $\phi$  in the bulk comoving frame. We first assume an isotropic distribution and calculate the light curve. The result is shown in Figure 1(a). One can immediately see that the light curve has a broad component, with some spiky small pulses superposed on top. The broad component is due to the contributions of all the mini-jets beaming toward random directions in the bulk motion rest frame. The rising of the broad pulse corresponds to the exponential growth of the number of mini-jets, while the decay is controlled by the high-latitude effect.

Since an ICMART event corresponds to an event of destroying the initial ordered magnetic field, the magnetic configura-

tions in the ICMART region, even near the end of the cascade, should not be completely random. The initial magnetic field configuration should be parallel to the ejecta plane (e.g., Spruit et al. 2001; Zhang & Kobayashi 2005). This is because the toroidal component falls with radius much slower than the poloidal component. Such a configuration should still leave an imprint on the  $\phi$  distribution. We consider a distribution of  $\phi$  that has a Gaussian distribution with respect to the original field line direction, i.e.,  $\phi = 90^\circ$ . In Figures 1(b) and 1(c) we show the Gaussian angle to be  $45^\circ$  and  $30^\circ$ , respectively. One can see that the simulated light curves have progressively less flux as the distribution angle becomes smaller. This is because with a smaller distribution angle, only rare mini-jets could beam toward the observer, which have a relatively lower flux (than the larger Gaussian angle distribution) with respect to the majority of mini-jets that beam away from the observer and only contribute to the background. The overall shape of the light curves does not differ significantly.

### 3.1.2. Lorentz Factor Contrast

We next compare the effect of Lorentz factor contrast in the ICMART region. We keep the initial value of the bulk Lorentz factor  $\Gamma$  constant, i.e.,  $\Gamma_{\text{ini}} = 200$ , and vary  $\gamma_{\text{ini}}$ . This corresponds to different values of the initial magnetization  $\sigma_{\text{ini}}$ . In Figure 2, we compare three sets of simulations, with (a)  $\gamma_{\text{ini}} = 8$ ; (b)  $\gamma_{\text{ini}} = 14$  and (c)  $\gamma_{\text{ini}} = 20$ . Other parameters are the same as those adopted to calculate Figure 1, and the Gaussian  $\phi$ -distribution model with typical angle  $45^\circ$  has been adopted. We show that the light curves become progressively more erratic and spikier when the  $\gamma_{\text{ini}}$  becomes larger. This is because a larger  $\gamma_{\text{ini}}$  would give rise to larger  $\mathcal{D}_2$ , and thus a larger value of the total Doppler factor  $\mathcal{D}_1 \mathcal{D}_2$ . A larger  $\gamma_{\text{ini}}$  also tends to give a more significant evolution of the parameters (Figure 3). Initially, a constant  $\Gamma_{\text{ini}}$  corresponds to a constant  $1/\Gamma_{\text{ini}}$  cone, so that observed numbers of mini-jets are the same in all these cases. However a larger  $\gamma_{\text{ini}}$  can give rise to a larger  $\Gamma$  near the end of evolution, thus a smaller  $1/\Gamma$  cone. The slow component is not as significant, so that the light curves become spikier.

In order to show the evolution of the physical parameters during the ICMART cascade event, in Figure 3 we display the evolution of the bulk Lorentz factor  $\Gamma$ , the mini-jet Lorentz factor  $\gamma$ , and the emission region magnetization  $\sigma$  as a function of time. It can be seen that evolution is more significant for a larger  $\gamma_{\text{ini}}$  (and equivalently a larger  $\sigma_{\text{ini}}$ ).

### 3.1.3. Number of Reconnection Events

Next, we test how the total number of mini-jets  $N$  within the  $1/\Gamma$  cone affects the light curves. According to Equation 6, varying  $N$  is effectively varying the filling factor  $f$ . By varying  $N$ , the total number of e-folding steps  $n$  is slightly modified, as is the rising time  $t_r$ . In Figure 4, we compare the simulated light curves for different  $N$  values, i.e.,  $N = 10^4, 5 \times 10^4, 10^5$ , and  $5 \times 10^5$ , respectively. It can be seen that in general the light curves appear smoother with increasing  $N$ . This can be readily understood: the larger the  $N$ , the more reconnection events happen simultaneously, so that more mini-jets beaming to different directions tend to enhance the slow component. The short-timescale structures are smeared out, and the light curves become smoother.

### 3.1.4. Emission Radius

Next, we explore the effect of the emission region radius  $R$ . Figures 5(a), 5(b), and 5(c) show the results for  $R = 5 \times 10^{15}$

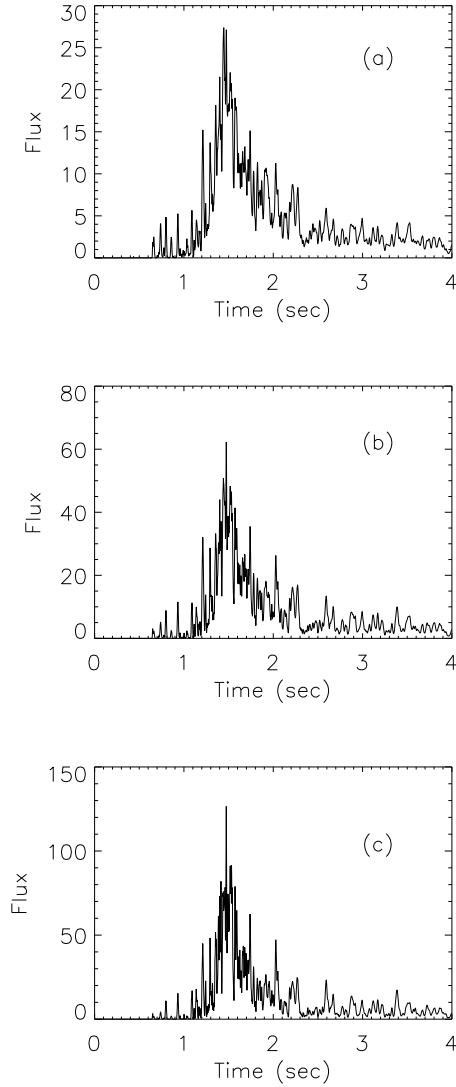


FIG. 2.— Simulated light curves of one ICMART event with the following parameters:  $R = 5 \times 10^{15}$  cm,  $\Gamma_{\text{ini}} = 200$ ,  $L' = 5 \times 10^{11}$  cm,  $N = 50,000$  and rising time  $t_r \sim 1.5$  s. The  $\phi$ -distribution is taken as Gaussian with typical angle  $45^\circ$ . Three panels compare different  $\gamma_{\text{ini}} - \Gamma_{\text{ini}}$  contrasts. (a)  $\gamma_{\text{ini}} = 8$ ; (b)  $\gamma_{\text{ini}} = 14$ ; (c)  $\gamma_{\text{ini}} = 20$ .

cm,  $R = 10^{15}$  cm, and  $R = 5 \times 10^{14}$ , respectively. One can see that the larger the  $R$ , the longer and stronger the high-latitude emission tail. This is because the length of the high-latitude tail is defined by  $R(1 - \cos\theta_j)$ . We notice again that the rising time is the growth time of the cascade, which is the  $e$ -folding time of consuming most of the magnetic energy in the emission region, which is defined by the total number  $N$  of the mini-jets and the characteristic scale  $L'$  of each mini-jet. Since the rising and falling times are related to different parameters, the pulse is usually asymmetric (e.g., Figure 5). The simulated light curve is more consistent with data if the emission radius  $R$  is large. ZY11 suggested that ICMART events should happen at larger radii, say,  $R > 10^{15}$  cm, in order to reach the critical condition of triggering a reconnection/turbulence cascade. It is intriguing to see that such large-radius ICMART events make light curves more resemble the

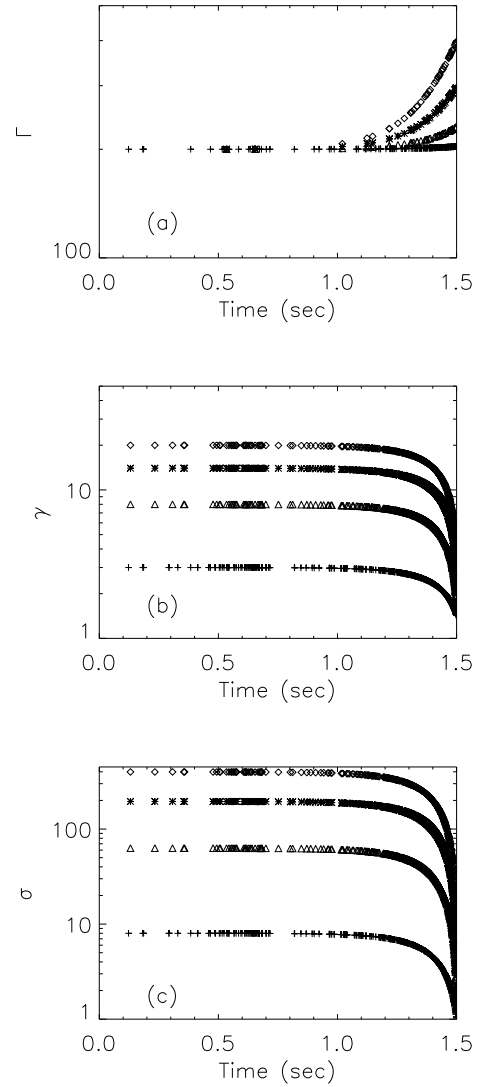


FIG. 3.— Evolution of the following parameters during the simulated ICMART event: (a)  $\Gamma$ ; (b)  $\gamma$ ; (c)  $\sigma$ . The different symbols denote different parameters presented in Figures 1 and 2: cross:  $\Gamma_{\text{ini}} = 200$ ,  $\gamma_{\text{ini}} = 3$ , triangle:  $\Gamma_{\text{ini}} = 200$ ,  $\gamma_{\text{ini}} = 8$ , star:  $\Gamma_{\text{ini}} = 200$ ,  $\gamma_{\text{ini}} = 14$ , diamond:  $\Gamma_{\text{ini}} = 200$ ,  $\gamma_{\text{ini}} = 20$ .

observed ones.

### 3.1.5. Size of the Reconnection Regions

We also discuss the effect of different sizes of reconnection regions. We make two sets of simulations. In the first set, we vary  $L'$  while keeping  $R$  constant. We also keep  $N = 50,000$ , so effectively, we are varying the filling factor  $f$ . Since  $t_0 = L'/v_{\text{in}}$ , the rising time  $t_r$  is modified correspondingly. The results are presented in Figure 6, which shows the simulated light curves for  $L' = 10^{10}$ ,  $10^{11}$ , and  $10^{12}$  cm, respectively. It can be seen that the smaller the  $L'$ , the spikier the light curve. This is because a smaller  $L'$  corresponds to a shorter duration of each reconnection event. For the  $L' = 10^{12}$  cm case, short-timescale structures are missing, and the light curve is very smooth.

Next, we keep both  $N$  and  $f$  constant. By varying  $L'$ , we are effectively varying  $R$  as well, so that the ratio  $L'/R$

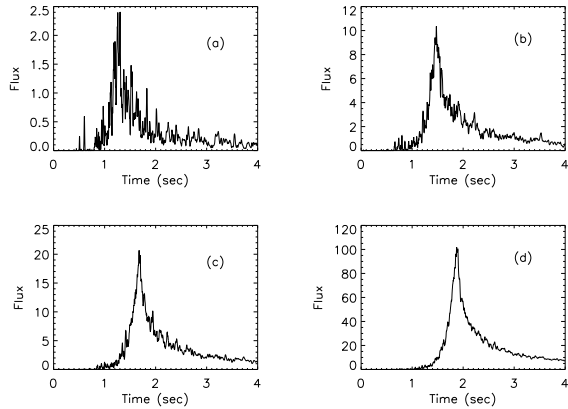


FIG. 4.— A comparison of the cases with different reconnection events  $N$ . The parameters are the same as those in Figure 1 except  $N$ . (a)  $N = 10^4$ ; (b)  $N = 5 \times 10^4$ ; (c)  $N = 10^5$ ; (d)  $N = 5 \times 10^5$ .

is a constant. The results are shown in Figure 7, in which light curves for  $L' = 10^{10}$ ,  $10^{11}$ , and  $10^{12}$  cm are simulated. The general trend as discussed above is still there, but since  $R$  is changed accordingly, the contrasts are less significant, namely, the smaller  $L'$  cases are less spiky and larger  $L'$  cases are less smooth with respect to the case where  $R$  is fixed (Figure 6). Since the decay phase is defined by  $R$  (Section 3.1.4 above), varying  $R$  with  $L'$  also affects the length of the decaying phase.

### 3.1.6. Size distribution

We next test the effect of size distribution of the reconnection regions. We try two possibilities: the power-law distribution with an index  $-5/3$  (the Kolmogorov type) (Figure 8(a)) and a uniform distribution (Figure 8(b)). One can see that the uniform distribution has a smoother shape. In this case, the observed small pulse width distribution is solely determined by the distribution of the Doppler factors. For the power-law distribution case, an extra factor (the intrinsic distribution) plays a role to make small pulses, so that the light curves are spikier.

### 3.1.7. Energy dependence

Finally we calculate the light curves for different energy bands. We consider three cases here, below the peak of the band spectrum (Figure 9(a)), i.e., 15 - 150 keV (also the observation band for *Swift* BAT), above the peak (500 - 650 keV, Figure 9(b)), and across the entire energy band (15 - 650 keV, Figure 9(c)). The high-energy light curve is slightly narrower and spikier, as observed in real GRBs. In general, the overall shape of the light curves does not differ significantly.

### 3.1.8. Multiple episodes

As suggested by ZY11, a real GRB light curve may consist of multiple ICMART events. In Figure 10, we simulate three emission episodes and superpose them together to make a mock GRB light curve. We have varied  $\Gamma_{\text{ini}}$  and  $\gamma_{\text{ini}}$  around the values  $\sim 200$  and  $\sim 3$ , respectively, with small fluctuations in different episodes. Other parameters are the same as those adopted in Figure 1 with a  $45^\circ$  Gaussian  $\phi$ -distribution. The simulated light curve shows reasonable features as observed in some GRBs. We note that in reality the parameters of different ICMART events could be more different, so that

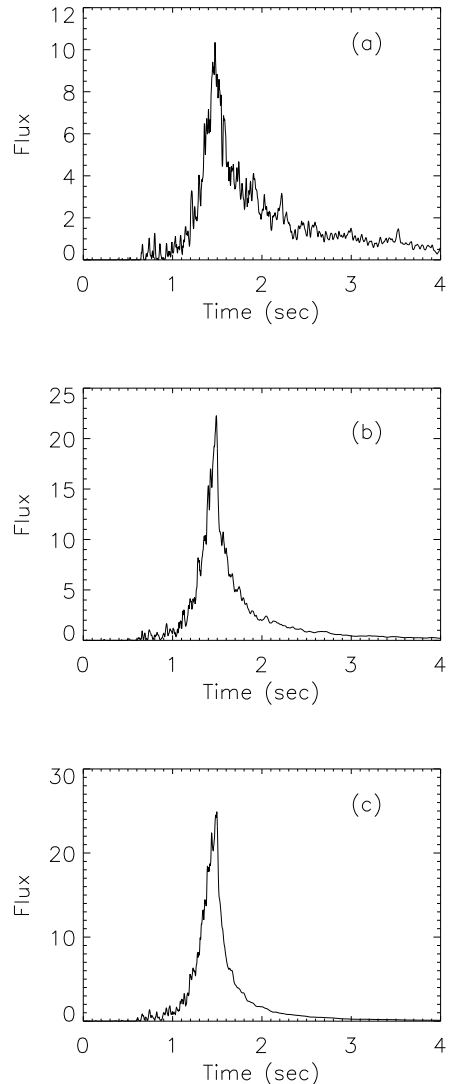


FIG. 5.— The simulated light curves with different emission region radius  $R$ : (a)  $R = 5 \times 10^{15}$  cm, (b)  $R = 10^{15}$  cm, and (c)  $R = 5 \times 10^{14}$  cm. The other parameters are the same as those in Figure 1.

a variety of light curves could be made, which may account for the diverse prompt emission light curves as observed.

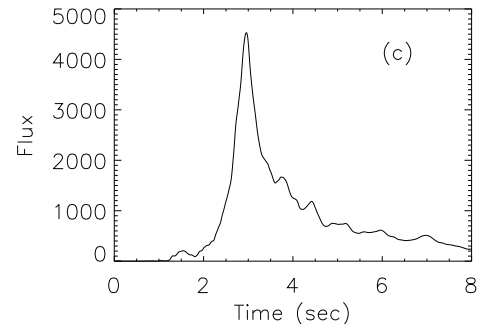
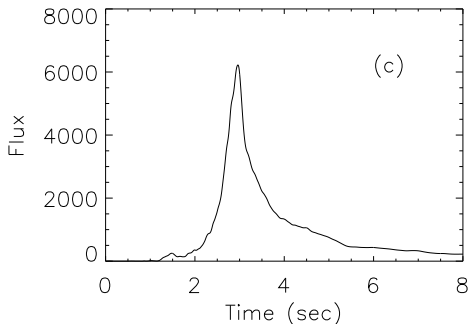
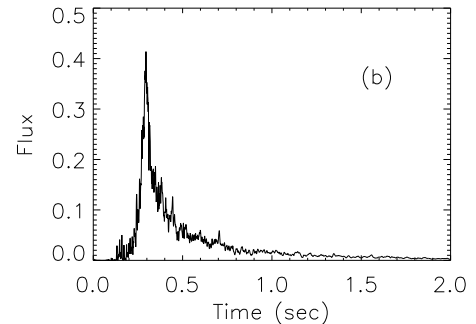
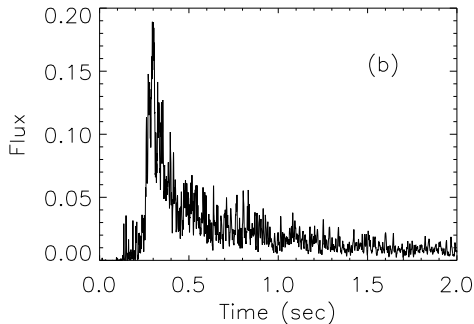
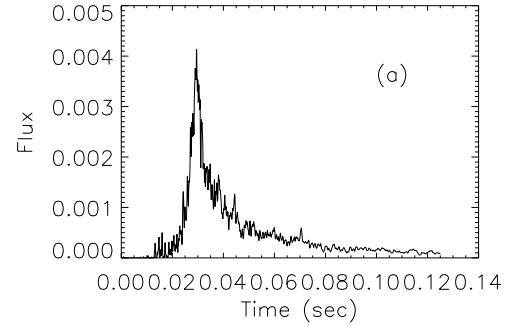
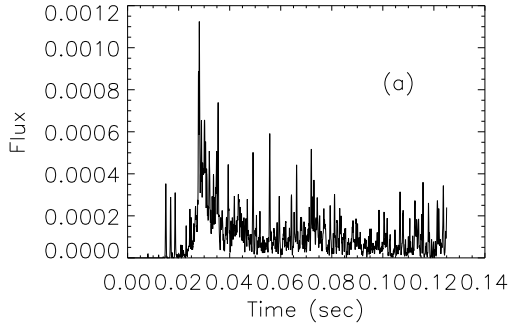


FIG. 6.— The simulated light curves with different size of reconnection region  $L'$ : (a)  $L' = 10^{10}$  cm, (b)  $L' = 10^{11}$  cm, and (c)  $L' = 10^{12}$  cm. The other parameters are the same as those in Figure 1.

FIG. 7.— The simulated light curves with different size of reconnection region  $L'$ , while keeping  $L'/R$  constant: (a)  $L' = 10^{10}$  cm, (b)  $L' = 10^{11}$  cm, and (c)  $L' = 10^{12}$  cm. The other parameters are the same as those in Figure 1.

### 3.2. Power Density Spectrum (PDS) Analysis

In order to test whether our simulated light curves mimic the observed ones, we also perform a PDS analysis of our results. In order to get robust PDS slopes, for each set of parameters, we perform 10 different Monte Carlo simulations to get 10 different light curves, derive the PDS slope of each light curve, and calculate the average slope to stand for this particular set of parameters. Some examples of PDSs are presented in Figure 11. Generally, the PDSs can be fit with a power law, with indices generally steeper than  $-1.8$ . The averaged PDS indices for all the cases corresponding to Figures 1, 2, and 4-9 are collected in Table 1. Observationally the PDS slopes are steeper in softer bands (e.g. *Swift*; Guidorzi et al. 2012) than harder bands (e.g. BATSE; Beloborodov et al. 2000). Our simulations recover this trend. The presented PDS values are taken from the *Swift* band. It is encouraging to see that the simulated values are generally consistent with the *Swift* data (Guidorzi et al. 2012). Our simulations also show a turnover

of PDSs in the high-frequency regime with a steeper index. Such a feature is seen in some GRBs.

From Table 1, one can see that various parameters can affect the slope of a PDS. Generally speaking, spikier light curves have more power in high frequencies and therefore have a shallower PDS slope. Most PDS indices listed in Table 1 can be understood this way. For Figure 1, it is seen that more isotropic distributions give steeper slopes. This is because the more isotropic cases give more mini-jets contributing to the broad component, and thus enhance the low-frequency power. Similarly, as shown in Figure 4, a smaller number  $N$  gives richer spiky features, and therefore gives a shallower PDS slope. The  $R$ -dependence (Figure 5) can be understood as the following: a larger  $R$  corresponds to a longer curvature decay tail, on top of which rapid variability can be observed, so that the PDS slope is shallower. For the size effect (Figure 6), a smaller  $L'$  can give rise to pulses with shorter dura-

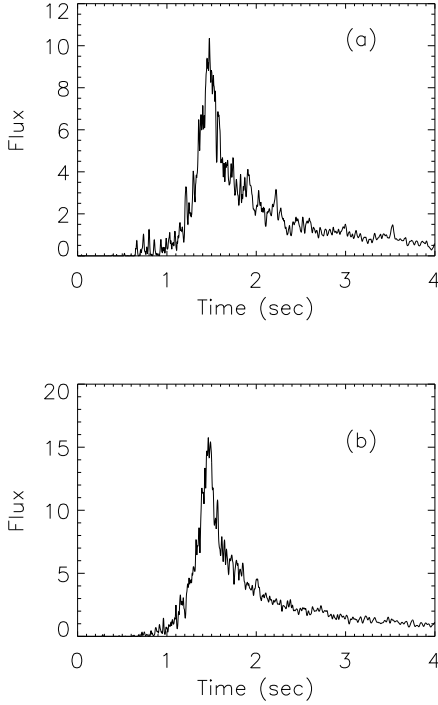


FIG. 8.— The simulated light curves with different reconnection region size distribution: (a) power law distribution with an index of  $-5/3$ ; (b) uniform distribution. The other parameters are the same as those in Fig. 1.

TABLE 1  
PDS SLOPES OF SIMULATED LIGHT CURVES

Figure	Slope
1(a)	-1.84
1(b)	-1.83
1(c)	-1.78
2(a)	-1.41
2(b)	-1.20
2(c)	-1.11
4(a)	-1.16
4(b)	-1.83
4(c)	-2.15
4(d)	-2.64
5(a)	-0.93
5(b)	-1.76
5(c)	-3.37
6(a)	-2.15
6(b)	-2.36
6(c)	-3.23
7(a)	-1.83
7(b)	-2.35
7(c)	-2.61
8(a)	-1.83
8(b)	-2.18
9(a)	-1.83
9(b)	-1.71
9(c)	-1.78

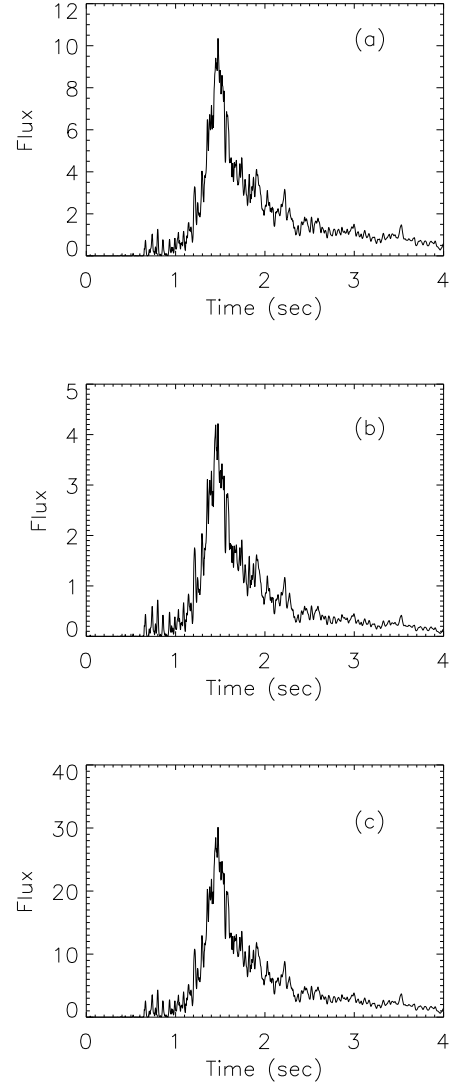


FIG. 9.— The simulated light curves in different observing bands: (a) 15 - 150 keV; (b) 500 - 650 keV; (c) 15 - 650 keV. The other parameters are the same as those in Figure 1.

tion and hence, a more dominant high-frequency power and shallower PDS (Figure 6). When both  $R$  and  $L'$  co-vary, this effect is still relevant, but somewhat compensated by the  $R$  effect (Figure 7). Next, without a size distribution, the PDS is steep (Figure 8(b)). By introducing a size distribution, one has more contributions to short-time variability from smaller sizes, so the PDS becomes shallower. Finally, the light curves in a higher energy band are somewhat spikier (Figure 9) and hence have a shallower PDS. This is consistent with the finding of Guidorzi et al. (2012) and Beloborodov et al. (2000): using the *Swift* BAT data, Guidorzi et al. (2012) obtained a steeper PDS slope than Beloborodov et al. (2000), who used the BATSE data (higher energy band) to perform the analysis.

It is interesting to investigate the change of PDS slope due to the change of the initial Lorentz factor contrast. As shown in Figure 3, in principle one can have strong parameter evolution during one ICMART event, which causes complicated evolution of the PDS behavior. To avoid such strong evo-

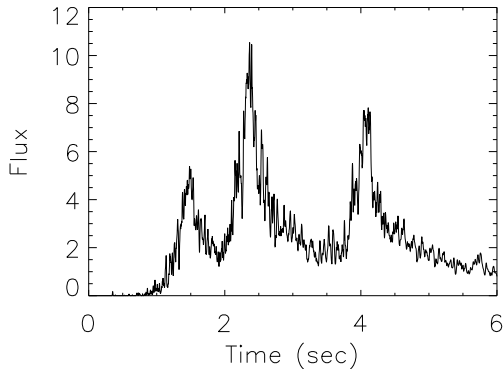


FIG. 10.— The Light curve of a GRB with three ICMART episodes. The parameters of each episode are close to those adopted in Fig. 1b.

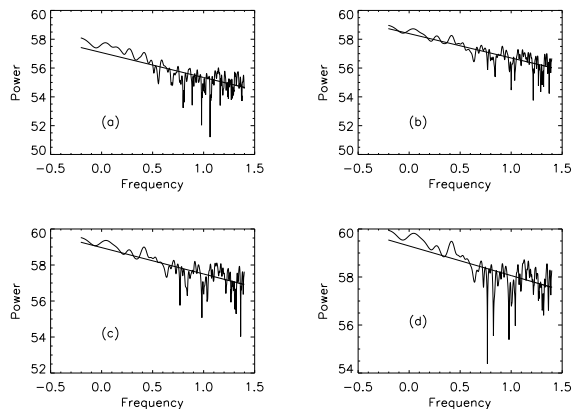


FIG. 11.— Power density spectrum (PDS) of sample light curves. A  $\phi$ -Gaussian distribution with typical angle  $45^\circ$  has been adopted. The parameters are: top left:  $\Gamma_{\text{ini}} = 200$ ,  $\gamma_{\text{ini}} = 3$ , with power law index  $p = -1.73$ ; top right:  $\Gamma_{\text{ini}} = 200$ ,  $\gamma_{\text{ini}} = 8$ ,  $p = -1.48$ ; bottom left:  $\Gamma_{\text{ini}} = 200$ ,  $\gamma_{\text{ini}} = 14$ ,  $p = -1.31$ ; bottom right:  $\Gamma_{\text{ini}} = 200$ ,  $\gamma_{\text{ini}} = 20$ ,  $p = -1.20$ . Other parameters are the same as Figure 1(a). Note that these values differ from those in Table 1, since the values in Table 1 are the averaged PDS slopes of 10 light curves.

lution, we first fix  $\Gamma_{\text{ini}} = 200$ , and vary  $\gamma_{\text{ini}}$  so that the ratio  $\gamma_{\text{ini}}/\Gamma_{\text{ini}}$  evolves in the range of 0.01–0.1. In Figure 12, we present the PDS slope as a function of  $\gamma_{\text{ini}}/\Gamma_{\text{ini}}$ . The triangles (and dotted line) are calculated by turning off parameter evolution (i.e., keeping  $\gamma$  and  $\Gamma$  unchanged throughout), and the squares (and solid line) are calculated by turning on the parameter evolution (Figure 3). One can see that the PDS slope becomes progressively shallower as  $\gamma_{\text{ini}}/\Gamma_{\text{ini}}$  increases. This is understandable, since a larger  $\gamma_{\text{ini}}$  corresponds to a stronger fast emission component, and therefore the light curves are spikier (see Figure 2). One can tentatively draw the conclusion that a more magnetized outflow tends to make spikier light curves.

Since the final Lorentz factor of the ejecta at the deceleration time is proportional to  $\Gamma_{\text{ini}}\gamma_{\text{ini}}$ , and since observationally the Lorentz factor at the onset of afterglow does not have a wide distribution (e.g., Liang et al. 2010), it is interesting to investigate how the PDS slope depends on the Lorentz factor contrast when  $\Gamma_{\text{ini}}\gamma_{\text{ini}}$  is set to constant. In Figure 13, we

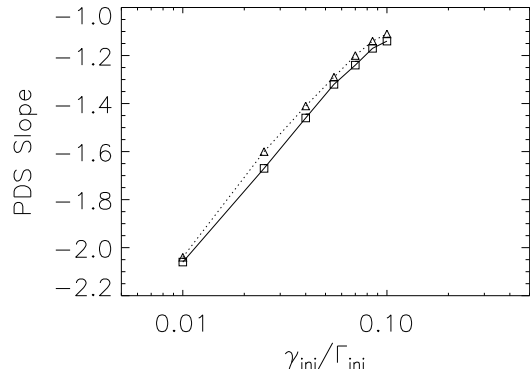


FIG. 12.— The PDS slope for different Lorentz factor contrast with a fixed  $\Gamma = 200$ . The triangles represent the PDS slopes of sample light curves without introducing parameter evolution. The dotted line connects the data points and gives the general trend of dependence. The squares and the solid line represent the PDS slopes as a function of Lorentz factor contrast when parameter evolution is taken into account.

present the case of  $\Gamma_{\text{ini}}\gamma_{\text{ini}} = 600$  for cases both without and with parameter evolution. The range of the contrast is set to  $\gamma_{\text{ini}}/\Gamma_{\text{ini}} = 1/150$  (i.e.  $\Gamma_{\text{ini}} = 300$ ,  $\gamma_{\text{ini}} = 2$ ) to  $\gamma_{\text{ini}}/\Gamma_{\text{ini}} = 1.5$  (i.e.,  $\Gamma = 20$ ,  $\gamma = 30$ ). The convention is the same as Figure 10. The dependence shows more complicated patterns. For the case without evolution (triangles and dotted line), in general one can see decrease of PDS slope when  $\gamma_{\text{ini}}/\Gamma_{\text{ini}}$  increases (except the slight tilt at very large  $\gamma_{\text{ini}}/\Gamma_{\text{ini}}$ ). This can be understood in the following way. As  $\gamma_{\text{ini}}/\Gamma_{\text{ini}}$  increases, one has two competing effects. The increase of  $\gamma_{\text{ini}}$  tends to enhance the small timescale variability. On the other hand, the decrease of  $\Gamma$  tends to enlarge the  $1/\Gamma$  cone, so that many more mini-jets not beaming toward the observer could contribute to the slow component. The net result after competition is that the latter effect wins, so that the long-time variability is more enhanced, and hence, a steeper PDS is obtained. This trend is overturned when  $\gamma_{\text{ini}}$  exceeds  $\Gamma_{\text{ini}}$  near the end of the curve.

When evolution is taken into account (squares and solid line), the situation is even more complicated. When  $\gamma_{\text{ini}}$  is small enough, the above-mentioned trend is retained. However, when  $\gamma_{\text{ini}}$  becomes large enough, evolution of  $\gamma$  and  $\Gamma$  becomes significant (Figure 3), so that quickly one can reach a regime with small  $\gamma$  and large  $\Gamma$ . The average PDS would be dominated by this late phase, so that the general trend is reversed from the no-evolution case. In reality, since a real GRB light curve would usually be the superposition of multiple ICMART events, the clean evolution expected in a single ICMART event would be smeared out.

#### 4. SUMMARY AND DISCUSSIONS

In this paper we have simulated a sample of GRB prompt emission light curves and PDSs within the framework of the ICMART model (ZY11). This model was developed to model GRBs whose jet composition is still somewhat Poynting flux dominated in the emission region. This was motivated by the non-detection of the photosphere component in some GRBs (Zhang & Pe'er 2009; Zhang et al. 2011). Since the emission region has a moderately high  $\sigma$ , in order to generate a reconnection/turbulence cascade envisaged by ZY11, the energy dissipation region must have many locally Lorentz-boosted emission regions, or mini-jets. The detected emis-

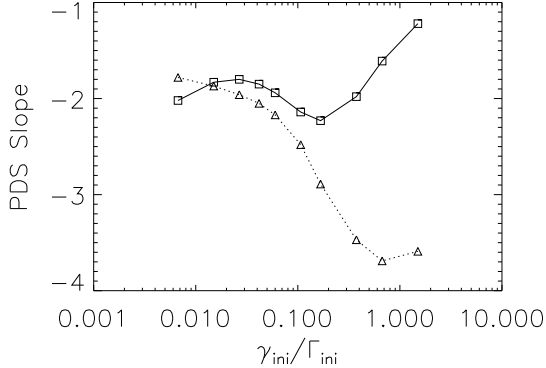


FIG. 13.— The PDS slope as a function of  $\gamma_{\text{ini}}/\Gamma_{\text{ini}}$  for a fixed value of  $\Gamma_{\text{ini}}\gamma_{\text{ini}} = 600$ . The triangles represent the PDS slopes of sample light curves without introducing parameter evolution. The dotted line connects the data points and gives the general trend of dependence. The squares and the solid line represent the PDS slopes as a function of Lorentz factor contrast when parameter evolution is taken into account.

sion would be the superposition of emissions from all these mini-jets, which beam to random directions in the bulk comoving frame. Other global magnetic dissipation models for GRB prompt emission have been proposed in the literature (e.g., Lyutikov & Blandford 2003; Giannios & Spruit 2006). If these models invoke runaway generation of mini-jets at a relatively large emission radius, then the simulations in this paper also apply to those scenarios.

Lacking detailed numerical simulations for a reconnection/turbulence cascade, we carried out a Monte Carlo simulation by inputting many mini-jets with certain directional and temporal distributions within the ICMART scenario. We investigated the roles of the directional distribution, Lorentz factor contrast, number of reconnection regions, emission radius, size of the mini-jet, mini-jet size distribution, energy dependence, etc., in defining the light curves and their PDSs. We adopt our simulation parameters according to observations (e.g., typical length of reconnection region  $L' = 5 \times 10^{11}$  cm corresponding to observed variability timescale  $t_0 \sim 0.1$  s, 15 - 150 keV band for simulated light curves corresponding to *Swift* BAT band, and so on), as well as the requirements of the ICMART model itself (e.g., emission region radius  $R = 5 \times 10^{15}$  cm in order to make sure that runaway reconnection can happen, and exponential growth of the number of reconnection events with time). Within the ICMART framework, most of our parameters are physically related to each other self-consistently.

Even though some simplified assumptions are introduced so that the light curves may not fully represent the complex physics in an ICMART event, our simulated light curves nonetheless show some encouraging features that are consistent with the GRB prompt emission data. The most noticeable feature is the superposition of an underlying slow component and more erratic fast component, which seems to be consistent with the data (Gao et al. 2012; Vetere et al. 2006). The slow component is caused by the superposition of emission from all the mini-jets in the emission region, while the fast component is related to those mini-jets that happen to beam toward the observer. We follow the physics of an ICMART event, including the exponential growth of the reconnection region,

dissipation of the magnetic field energy (so that  $\sigma$  drops with time), and acceleration of the bulk ejecta during the energy dissipation process and find that the erratic GRB light curves as observed can be generally reproduced within the model. Among all the model parameters, the Lorentz factor contrast and the number of mini-jets play an important role in defining the “spikiness” of the light curve. We also derived the PDS slopes of the simulated light curves, and found that they are generally consistent with the data. Generally speaking, the larger the contrast  $\gamma_{\text{ini}}/\Gamma_{\text{ini}}$  (keeping  $\Gamma_{\text{ini}}$  constant), the shallower the PDS slope.

Besides GRBs, the “jet-in-the-jet” scenario has been discussed in other astrophysical contexts. Giannios et al. (2010) interpreted the fast TeV variability of active galactic nucleus jets using the mini-jet scenario. Yuan et al. (2011) applied the scenario to account for the gamma-ray flares of the Crab Nebula. Compared with earlier work of Narayan & Kumar (2009), Kumar & Narayan (2009), and Lazar et al. (2009), the new ingredient introduced in our paper is the exponential growth of the number of mini-jets as a function of time, as envisaged in the ICMART model (ZY11; see also Stern & Svensson 1996). As a result, our model allows many mini-jets emitting simultaneously at any instant. This is the key ingredient to define the broad component of each ICMART event.<sup>10</sup> A GRB light curve is composed of multiple ICMART events (Figure 8), which are controlled by the erratic central engine activity.

In order to set up the Monte Carlo simulations, we had to introduce a number of assumptions. These include power-law distribution of the size of reconnection regions, Gaussian shape of each pulse, same intrinsic radiation spectrum for all emitters, exponential growth of numbers of pulses with time, isotropic or Gaussian distribution of the mini-jet directions, and so on. Some factors are still missing. For example, in the comoving frame of the jet bulk but outside the mini-jets, there would also be particles that give rise to radiation. The effects of this inter-mini-jet emission should be investigated (e.g., Lin et al. 2013).

The physical conditions of real GRBs must be more complex than what is modeled here, so that one may not reproduce the full observational features of GRBs with the simulations presented in this paper. Nonetheless, our simulations show the encouraging results that the simulated light curves based on these simplified assumptions can indeed reproduce some key features of the observations, e.g. the slow and fast variability components and a variety of degree of spikiness of the light curves. By changing parameters (e.g.,  $\phi$ -distribution, Lorentz factor contrast, jet opening angle), diverse light curves can be generated, ranging from relatively smooth to relatively spiky ones. The PDSs of the simulated light curves are also generally consistent with the data. All these suggest that the ICMART model may be a good candidate to interpret GRB prompt emission.

Within the ICMART theoretical framework, the following constraints can be made to the model parameters. (1) To reproduce the general fast-rising slower decay shape of broad pulses, the emission radius should be relatively large ( $\sim 10^{15}$  cm and beyond). (2) Since many GRBs show high-amplitude rapid variability, the GRB initial magnetization parameter  $\sigma_{\text{ini}}$

<sup>10</sup> In contrast, the previous relativistic turbulence models (Narayan & Kumar 2009; Lazar et al. 2009) only introduced a filling factor in time, so that they rarely have multiple mini-jets emitting at any instant. So their simulated light curves are too spiky, and do not have a slow component.

in the emission region could be high (e.g., from several to hundreds). (3) The observed minimum variability timescale constrains that  $L'$  cannot be too large and has to be  $\leq 5 \times 10^{11}$  cm. (4) In order not to smear these peaks by overgenerating mini-jets, one also requires a filling factor  $f \ll 1$ , suggesting that in these cases the global  $\sigma$  of the outflow after the ICMART event may not drop to unity. (5) Erratic light curves with multiple episodes suggest that the GRB central engine acts multiple times to eject highly magnetized shells so that multiple ICMART events can be generated within one burst. (6) The existence of smooth-pulse GRBs suggests that in some cases the  $\sigma_{\text{inj}}$  is not much larger than unity (so that  $\gamma_{\text{inj}}$

is not much larger than unity), or there are so many mini-jets operating simultaneously. Other information (e.g. polarization properties and prompt emission efficiency) is needed to break the degeneracy.

We thank Kohta Murase, Pawan Kumar, Zi-Gao Dai, He Gao, Da-Bin Lin, and Chun Li for useful discussion, and an anonymous referee for very helpful suggestions. This work is partially supported by NSF through grant AST-0908362. Bo Zhang acknowledges a scholarship from China Scholarship Council for support.

#### REFERENCES

- Amati, L., Frontera, F., Tavani, M., et al. 2002, *A&A*, 390, 81  
 Band, D., Matteson, J., Ford, L., et al. 1993, *ApJ*, 413, 281  
 Beloborodov, A. M., Stern, B. E., & Svensson, R. 2000, *ApJ*, 535, 158  
 Cho, J., Lazarian, A., & Vishniac, E. T. 2003, *Turbulence and Magnetic Fields in Astrophysics*, 614, 56  
 Daigne, F., & Mochkovitch, R. 1998, *MNRAS*, 296, 275  
 Daigne, F., & Mochkovitch, R. 2002, *MNRAS*, 336, 1271  
 Dermer, C. D., & Mitman, K. E. 1999, *ApJ*, 513, L5  
 Drenkhahn, G. & Spruit, H. C. 2002, *A&A*, 391, 1141  
 Fishman, G. J., & Meegan, C. A. 1995, *ARA&A*, 33, 415  
 Gao, H., Zhang, B.-B., & Zhang, B. 2012, *ApJ*, 748, 134  
 Giannios, D., & Spruit, H. C. 2006, *A&A*, 450, 887  
 Giannios, D., Uzdensky, D. A., & Begelman, M. C. 2010, *MNRAS*, 402, 1649  
 Ghisellini, G., Celotti, A., & Lazzati, D. 2000, *MNRAS*, 313, L1  
 Goldreich, P., & Sridhar, S. 1995, *ApJ*, 438, 763  
 Guidorzi, C., Margutti, R., Amati, L., et al. 2012, *MNRAS*, 422, 1785  
 Hascoët, R., Daigne, F., & Mochkovitch, R. 2012, *A&A*, 542, L29  
 Kobayashi, S., Piran, T., & Sari, R. 1997, *ApJ*, 490, 92  
 Kumar, P. 1999, *ApJ*, 523, L113  
 Kumar, P., & McMahon, E. 2008, *MNRAS*, 384, 33  
 Kumar, P., & Narayan, R. 2009, *MNRAS*, 395, 472  
 Lazar, A., Nakar, E., & Piran, T. 2009, *ApJ*, 695, L10  
 Lazarian, A., & Vishniac, E. T. 1999, *ApJ*, 517, 700  
 Lei, W.-H., Zhang, B., & Liang, E.-W. 2013, *ApJ*, 765, 125  
 Liang, E.-W., Yi, S.-X., Zhang, J., et al. 2010, *ApJ*, 725, 2209  
 Lin, D.-B., Gu, W.-M., Hou, S.-J., Liu, T. Sun, M.-Y., Lu, J.-F. 2013, *ApJ*, 776, 41  
 Lyubarsky, Y. E. 2005, *MNRAS*, 358, 113  
 Lyutikov, M., & Blandford, R. 2003, *arXiv:astro-ph/0312347*  
 Narayan, R., & Kumar, P. 2009, *MNRAS*, 394, L117  
 Panaitescu, A., Spada, M., & Mészáros, P. 1999, *ApJ*, 522, L105  
 Rees, M. J., & Meszaros, P. 1994, *ApJ*, 430, L93  
 Sari, R., & Piran, T. 1997, *ApJ*, 485, 270  
 Shen, R.-F., & Zhang, B. 2009, *MNRAS*, 398, 1936  
 Spruit, H. C., Daigne, F., & Drenkhahn, G. 2001, *A&A*, 369, 694  
 Stern, B. E., & Svensson, R. 1996, *ApJ*, 469, L109  
 Tagliaferri, G., Goad, M., Chincarini, G., et al. 2005, *Nature*, 436, 985  
 Uhm, Z. L., & Zhang, B. 2013, *arXiv:1303.2704*  
 Vetere, L., Massaro, E., Costa, E., Soffitta, P., & Ventura, G. 2006, *A&A*, 447, 499  
 Yamazaki, R., Ioka, K., & Nakamura, T. 2004, *ApJ*, 607, L103  
 Yuan, Q., Yin, P.-F., Wu, X.-F., et al. 2011, *ApJ*, 730, L15  
 Zhang, B., & Mészáros, P. 2002, *ApJ*, 581, 1236  
 Zhang, B., & Kobayashi, S. 2005, *ApJ*, 628, 315  
 Zhang, B., Fan, Y. Z., Dyks, J., et al. 2006, *ApJ*, 642, 354  
 Zhang, B., & Pe'er, A. 2009, *ApJ*, 700, L65  
 Zhang, B., & Yan, H. 2011, *ApJ*, 726, 90 (ZY11)  
 Zhang, B.-B., Zhang, B., Liang, E.-W., et al. 2011, *ApJ*, 730, 141  
 Zrake, J., & MacFadyen, A. I. 2012, *ApJ*, 744, 32  
 Zweibel, E. G., & Yamada, M. 2009, *ARA&A*, 47, 291